HHS Public Access

Author manuscript

Sens Actuators B Chem. Author manuscript; available in PMC 2025 March 28.

Published in final edited form as:

Sens Actuators B Chem. 2024 August 15; 413: . doi:10.1016/j.snb.2024.135839.

Activatable near-infrared fluorescence and chemical exchange saturation transfer MRI multimodal imaging probe for tumor detection in vitro and in vivo

Sanu Karan[a,1], **Jee-Hyun Cho**[b,1], **Chau Thi Ngoc Tran**[a,c], **Mi Young Cho**[a], **Hyunseung Lee**[a], **Rema Naskar**[d], **Inkyu Hwang**[d], **Sourav Pradhan**[e], **Hye Sun Park**[a], **Eun Hee Han**[a], **Jonathan L. Sessler**[f,*], **Kwan Soo Hong**[a,c,g,**]

[a]Biopharmaceutical Research Center, Korea Basic Science Institute, Cheongju 28119, Republic of Korea

[b]Center for Bio-imaging and Translational Research, Korea Basic Science Institute, Cheongju 28119, Republic of Korea

[c]Graduate School of Analytical Science and Technology, Chungnam National University, Daejeon 34134, Republic of Korea

[d]Immunology and Immunopharmacology Laboratory, College of Pharmacy, Chungnam National University, Daejeon 34134, Republic of Korea

[e]Department of Chemistry, Korea Advance Institute of Science and Technology (KAIST), Daejeon 34134, Republic of Korea

[f]Department of Chemistry, The University of Texas at Austin, Austin, TX 78712-1224, USA

[g]Department of Chemistry, Chung-Ang University, Seoul 06974, Republic of Korea

Abstract

Multimodal imaging has emerged as a powerful tool in biomedical research and clinical diagnostics. Ideally, it combines multiple imaging techniques to provide complementary anatomical and molecular information in living subjects. Particularly desirable are multimodal

*Corresponding author. sessler@cm.utexas.edu (J.L. Sessler). **Corresponding author at: Biopharmaceutical Research Center, Korea Basic Science Institute, Cheongju 28119, Republic of Korea. kshong@kbsi.re.kr (K.S. Hong).

[1]These authors contributed equally to this work.

CRediT authorship contribution statement

Chau Thi Ngoc Tran: Methodology, Investigation, Data curation. **Mi Young Cho:** Validation, Methodology, Formal analysis, Data curation. **Kwan Soo Hong:** Writing – review & editing, Supervision, Project administration, Investigation, Funding acquisition. **Sanu Karan:** Writing – original draft, Validation, Investigation, Data curation, Conceptualization. **Jee-Hyun Cho:** Writing – original draft, Methodology, Investigation, Data curation. **Eun Hee Han:** Visualization, Validation, Methodology. **Jonathan L. Sessler:** Writing – review & editing, Project administration, Funding acquisition, Conceptualization. **Sourav Pradhan:** Software, Methodology, Formal analysis. **Hye Sun Park:** Visualization, Methodology, Data curation. **Inkyu Hwang:** Supervision, Investigation. **Hyunseung Lee:** Visualization, Methodology, Investigation, Data curation. **Rema Naskar:** Visualization, Methodology, Data curation.

Appendix A. Supporting information

Supplementary data associated with this article can be found in the online version at doi:10.1016/j.snb.2024.135839.

Declaration of Competing Interest

The authors declare that they have no known competing financial interests or personal relationships that could have appeared to influence the work reported in this paper.

imaging probes capable of providing differential diagnostic signals upon interaction with specific molecular targets. Hydrogen peroxide (H_2O_2) is a key target in this regard, since it is typically overexpressed in cancer cells. In this study, we present a small-molecule probe that not only selectively detects endogenous H_2O_2 through multimodal imaging, with a significant H_2O_2-triggered 15-fold fluorescence enhancement but also turns “on” a chemical exchange saturation transfer (CEST) magnetic resonance (MR) response with 60-fold signal enhancement at pH 7.4. Excellent selectivity against various other biologically relevant species is seen. Using this probe, we observed 3.4–4.5-fold and 2.8–5.8-fold higher H_2O_2 levels in cancerous cell lines and tumor tissues compared to normal cell lines and tissues, respectively. Time-dependent in vivo fluorescence and CEST imaging in a HeLa (Henrietta Lacks) tumor xenograft mouse model revealed probe-dependent tumor detection by fluorescence and CEST MRI contrast in the tumor area. These observations are attributed to the relatively high endogenous H_2O_2 levels produced during mitosis. This newly developed probe holds promise for advancing our understanding of H_2O_2-related biology and for cancer detection both in vitro and in vivo.

Keywords

Multimodal; Diagnosis; Cancer; CEST; Fluorescence; Luminescence

1. Introduction

Molecular imaging has emerged as a versatile and indispensable tool for modern biological research and disease diagnosis. By providing insights into biology fundamentals and providing enhanced disease diagnostic capabilities, molecular imaging has transformed our understanding of basic biology and improved healthcare outcomes [1,2]. Various techniques, including fluorescence imaging (FI), magnetic resonance imaging (MRI), single-photon emission computed tomography (SPECT), positron emission tomography (PET), ultrasound imaging (USI), computed tomography (CT), and photoacoustic imaging (PAI), have been developed in an effort to permit and improve in vivo molecular imaging [3,4].

Each imaging method has unique advantages and inherent limitations [5,6]. For example, FI has high sensitivity, ease of use, affordability, and rapid image acquisition [7,8]. However, shallow tissue penetration and susceptibility to interference from biological tissues limits its effectiveness. In contrast, PET offers extraordinary sensitivity and deep tissue penetration but is hindered by its poor spatial resolution [9–11]. MRI, allows remarkable spatial resolution and good tissue penetration; it excels in providing high-quality three-dimensional (3D) images but falls short in terms of sensitivity [12]. Photoacoustic imaging (PAI), a recently introduced technique that produces three-dimensional (3D) images with exceptional sensitivity, spatial resolution, and deeper tissue penetration [13,14], suffers from limitations when visualizing biomolecules deeply seated within the human body [15,16]. So-called multimodal molecular imaging offers a potential solution to the limitations of individual imaging techniques. By combining two or more imaging modalities, multimodal imaging harnesses the inherent characteristics of each modality and thus has the potential to yield detailed anatomical and cellular information. Multimodal molecular imaging thus holds the promise of enhancing our understanding of biological processes and improving our

ability to monitor disease pathogenesis [17,18]. However, for the promise of multimodal molecular imaging to be realized new probes that enhance the sensitivity of complementary imaging methods need to be developed. Here, we report the preparation and study of a multimodal imaging probe, **BODIPY-perox** that acts as a combined cancer specific long near-infrared (NIR) luminescent chemical exchange saturation transfer (CEST) magnetic resonance imaging (MRI) agent both in vitro and in vivo (Scheme 1). As shown in Scheme 2, **BODIPY-perox** is comprised of two distinct moieties, namely the NIR fluorescent emitter BODIPY and a hydrogen peroxide (H_2O_2)-responsive linker that upon reaction releases a free phenolate hydroxyl (-OH) group to enhance CEST MRI. A control system, **DOTA-perox**, was also prepared. It contains an Eu-chelating DOTA core and a H_2O_2 sensing subunit. However, in contrast to **BODIPY-perox** it lacks a fluorophore.

H_2O_2 is a quintessential reactive oxygen species (ROS) generated primarily by active triphosphopyridine nucleotide (NADPH) oxidase in cells [19,20]. H_2O_2 plays a crucial role as a messenger in cellular signal transduction for various physiological functions and serves as a marker for oxidative stress [21,22]. Its synthesis in cellular organelles, particularly within mitochondria, is essential for cell survival, proliferation, differentiation, and maintenance under normal conditions [23,24]. However, abnormal H_2O_2 production or accumulation within cellular mitochondria due to oxidative stress and/or genetic abnormalities is linked to numerous diseases, including cancer, diabetes, obesity, stroke, and neurological disorders [25–28]. This dichotomy has motivated the development of innovative tools for localizing and monitoring endogenous H_2O_2 production within cells.

MRI offers an appealing alternative to optical imaging due to its superior spatial resolution, substantial penetration depth, and lack of harmful radiation exposure. Chemical exchange saturation transfer (CEST) agents, with their distinctive magnetic resonance frequencies, facilitate precise detection of these agents and their associated biomarkers in comparison to traditional MRI techniques [29,30]. CEST agents operate by selectively reducing the magnetization of water signals while minimally affecting their longitudinal relaxation rate. Realizing these potential benefits requires the use of molecules with exchangeable protons in conjunction with the magnetization transfer nuclear magnetic resonance (MT-NMR) technique pioneered by Forsen and Hoffman in 1963 [31].

To date, various methods have been explored for H_2O_2 detection, with fluorescent probes standing out for their sensitivity in measuring endogenous H_2O_2 [32–34]. MRI-based H_2O_2 detection methods are also appealing; they offer excellent resolution but typically lack specificity and sensitivity for endogenous H_2O_2 (Fig. 1 and Table S1) [35–37]. Recent developments in sensing platforms and activatable luminescent chemical exchange saturation transfer (CEST) MRI probes have shown promise [38]. However, challenges persist, such as the limited reach of intravenously injected activatable luminescent MRI agents at tumor sites and a lack of specificity for H_2O_2. We posited that a probe that allowed the concurrent use of both techniques (fluorescence detection and CEST MRI) might provide for improved H_2O_2 detection and, accordingly, improved diagnoses of hydrogen peroxide-related pathologies. Using **BODIPY-perox** we show that this approach is effective in the context of cancer detection, both in vitro and in vivo. This success is ascribed to the presence of elevated H_2O_2 concentrations in the tumor micro-environment (TME).

2. Materials and methods

2.1. Materials and general experimental methods

Details are provided in the Supporting Information.

2.2. Synthesis of compound DOTA-perox

Compound **4** (759 mg, 1 mmol) was dissolved in TFA (2 mL) and stirred for 24 h. The mixture was evaporated to dryness. The resulting product was purified by silica gel column chromatography using dichloromethane/methanol (DCM/MeOH = 95:5) as the eluent, yielding a free ligand (410 mg). The free ligand (59 mg, 0.1 mmol) and K_2CO_3 (41 mg, 0.03 mmol) were dissolved in water (10 mL), and the pH was adjusted to 7 with NaOH (0.1 M). Excess $EuCl_3$•6 H_2O was added, and the pH was adjusted to 6.5. After stirring at room temperature for 12 h, the excess Eu^{3+} was precipitated as $Eu(OH)_3$ by increasing the pH above 8 using 1 M aqueous NaOH. The solution was filtered, and the pH was adjusted to 7 using 1 M HCl. The solution was freeze-dried to obtain **DOTA-perox** (68 mg, 91.9%). A xylenol orange indicator test was used to examine an aqueous solution of the Eu^{3+}-(**4**) complex for the absence of free Eu^{3+} ions. The purity of **DOTA-perox** was confirmed by a high performance liquid chromatography (HPLC) with a retention time (R_f) of 3.4 min being seen on a Sunfire C18 column (4.6 mm × 150 mm, 5 μm; Waters, MA, USA) and with a flow rate of 1 mL/min, resulting in 96.1%. ^{1}H NMR (400 MHz, DMSO-d_6): δ 7.86 (d, J = 6.64, 2 H); 7.797 (s, 2 H); 3.9 (s, 2 H); 3.515 (s, *6*H); 3.377 (d, J = 17.12, 6 H); 3.019 (m, 8 H); 2.799 (s, 2 H); 1.108 (s, 12 H). ^{13}C NMR (100 MHz, DMSO-d_6): 174.342, 133.869, 127.150, 117.80, 114.896, 75.605, 53.013, 51.703, 48.999, 47.653, 42.189, 23.677 ppm. ESI HRMS m/z[M+H]$^+$: calculated 764.199, found 764.197.

2.3. Synthesis of compound BODIPY-perox

To a solution of **6** (408 mg, 0.526 mmol) in DMF (2 mL), bis(pinacol) diboron (174 mg, 0.684 mmol) and potassium acetate (155 mg, 1.58 mmol) were added. The flask was purged with nitrogen gas for 15–20 min. Pd(dppf)Cl_2 (129 mg, 0.158 mmol) was added to the solution, and the reaction mixture was purged with nitrogen gas for another 10 min. The reaction mixture was stirred at 110 °C for 2 h. The volatiles were evaporated off, and the residual was extracted with ethyl acetate. The organic layer was dried over anhydrous sodium sulfate, and the crude product was purified by silica gel column chromatography using dichloromethane/methanol (DCM/MeOH = 95:5) as the eluent, yielding a dark green solid (298 mg, 76%). ^{1}H NMR (400 MHz, DMSO-d_6): δ 8.149 (m, 8 H), 8.06 (d, J = 10.68, 1 H), 7.461 (m, 7 H), 7.096 (d, J = 10.12, 1 H), 7.069 (m, 3 H), 4.614 (s, 2 H), 1.535 (s, 12 H), 1.396 (s, 9 H). ^{13}C NMR (100 MHz, DMSO-d_6). 167.47, 160.63, 146.245, 144.931, 142.786, 135.532, 134.791, 134.433, 132.593, 132.12, 131.451, 131.364, 129.61, 129.453, 129.408, 129.284, 129.186, 128.616, 128.584, 128.242, 126.221, 124.434, 119.398, 118.528, 114.923, 84.003, 82.792, 65.646, 28.067,24.903. ESI-HRMS m/z [M+H]$^+$: calcd. 754.336, found 754.3302.

3. Results and discussion

3.1. Design and synthesis of the DOTA-perox probe

The **DOTA-perox** control probe was synthesized as follows. A first key precursor, (4-(2-bromoacetyl)phenyl)boronic pinacol ester (compound **2**), was obtained by treating 4-acetylbenzeneboronic pinacol ester (compound **1**) with bromine in chloroform ($CHCl_3$) at room temperature (Scheme S1). A second precursor, compound **3**, was synthesized by selectively protecting 1,4,7,10-tetraazacyclododecane (CYCLEN) through triple *N*-alkylation with *tert*-butyl bromoacetate [39]. Compound **4** was then prepared by reacting **3** with **2**. Deprotecting the *tert*-butyl groups using trifluoroacetic acid yielded **DOTA-perox**. Treating this ligand with an excess of $EuCl_3 \cdot 6\ H_2O$ gave the corresponding Eu^{3+}-chelated complex. The key precursor to **BODIPY-perox**, compound **6**, was prepared by treating the known BODIPY derivative **5** [40] with triflic anhydride. Palladium(II)-mediated coupling with bis (pinacolato)diboron then yielded **BODIPY-perox**. Both probes and intermediates **1**–**5** were characterized by ^1H and ^{13}C NMR spectroscopy and HR-MS (Figures S1–S15).

Fig. 2 presents the DFT-optimized structures and frontier molecular orbitals for **DOTA-perox** (**A**) and **BODIPY-perox** (**B**). In both species, a presumed hydrogen-bonding interaction between the -BF_2 group and the phenyl ring is inferred based on their geometric proximity. The computed energy gaps between the highest occupied molecular orbital (HOMO) and the lowest unoccupied molecular orbital (LUMO) of **BODIPY-perox** and **DOTA-perox** were found to be 0.113 and 0.144 eV, respectively. These values lead us to suggest that **BODIPY-perox** is more reactive and sensitive than **DOTA-perox**. **BODIPY-perox**, as shown in Fig. 2C, exhibits sp^2 hybridization at the boron atoms [41]. When the nucleophile anionic form of hydrogen peroxide, O_2H^-, attacks the boron atom in **BODIPY-perox**, a boronate complex is generated with concurrent rehybridization to form a sp^3 hybridized boron center (**Int-1**). As a consequence of the high electron density on the boron atom, the C–B bond dissociates, followed by aryl migration to the adjacent oxygen acceptor atom to generate intermediate **Int-2**. The calculated activation energy ($\Delta G^{\neq}$) for this step (Int-1 → Int-2) is 24.54 kcal/mol for a pathway proceeding via inferred transition state **TS-1.** Hydrolysis of **Int-2** results in the formation of a phenolic –OH group and full cleavage of **BODIPY-perox**. The calculated $\Delta G^{\neq}$ for the rate-limiting step in the anionic O_2H^- oxidative pathway (Int-**1** → Int-**2**) is much lower than that computed for the neutral pathway, leading us to propose that the anionic pathway is energetically feasible and likely dominant [42]. We also optimized the transition state (TS) of oxidative conversion of the boronic ester to the electron-donating phenol of **BODIPY-perox** with a Gaussian 09 program. Geometry optimizations were performed using B3LYP-D3/6–31 G** (water, ε = 78.3553) B3LYP-D3/6–311+G** level of theory.

3.2. Optical properties of BODIPY-perox and DOTA-perox

To determine whether H_2O_2 could reduce the boronic ester or boronic acid moiety in the probes (**BODIPY-perox** and **DOTA-perox**) to their corresponding phenol (hydroxyl) forms, we monitored the changes in the UV–vis absorption spectra and fluorescence emission of the compounds in the presence of various concentrations of H_2O_2 under simulated physiological conditions. Initially, we recorded the UV absorbance spectrum of **BODIPY-**

perox dissolved in phosphate buffered saline (PBS) at different H_2O_2 concentrations (Fig. 3A). The UV–vis absorption maximum of probe **BODIPY-perox** (5 μM) at 700 nm increased in intensity by approximately 25-fold upon adding 200 μM H_2O_2, as illustrated in Fig. 3B. Similarly, the emission intensity at 730 nm increased 10-fold when exposed to 200 μM of H_2O_2 (Fig. 3C) with the changes proving concentration dependent (Fig. 3D). Specifically, the relative mean fluorescence intensity of **BODIPY-perox** (5 μM) was measured at different concentrations of H_2O_2 (0, 50, 100, 150, and 200 μM) using an optical imaging system (IVIS spectrum, Perkin Elmer) (Figs. 3G and 3H) with an increase in fluorescence intensity as a function of increasing H_2O_2 concentration being observed. The time required to reach fluorescence intensity saturation decreased with increasing H_2O_2 concentration with the maximum intensity being attained in most cases within approximately 12 min. The detection limit was determined to be 1.41 ng/mL. A HPLC analysis of probe **BODIPY-perox** (5 μM) in the presence of H_2O_2 revealed a new band, consistent with the H_2O_2-promoted reduction of the boronic ester group to a phenol (Fig. 3I). Further support for the proposed reaction between H_2O_2 and **BODIPY-perox** came from an HR-MS analysis carried out after treatment with 200 μM H_2O_2 at 37 °C for 30 min. A major $[M + H]^+$ peak was seen at 644.248 reflecting the generation of an activated probe[37] (Figure S16).

Before applying probe **BODIPY-perox** to an in vitro cellular test system, we examined whether other biologically relevant analytes, including metal ions (K^+, Mg^{2+}, Ca^{2+}), redox active species (ascorbic acid, vitamin B_6, human serum albumin (HSA), H_2O_2, and $S_2O_3^{2-}$), enzymes (lipase, pepsin, trypsin, and phosphatase), and amino acids (cystine, alanine, serine, lysine, histidine, arginine, glutamic acid, and tyrosine), gave rise to interference. No significant spectroscopic changes were observed in the presence of these potentially interfering analytes (Fig. 3E and F).

We also monitored changes in the fluorescence intensity of the probe at 730 nm in the presence of H_2O_2. The fluorescence intensity reached a maximum at an H_2O_2 concentration of 200 μM. These spectral changes are attributed to converting the boronic ester group into the corresponding phenol (–OH) group, which is an excellent electron donor. The resonance process results in the “turn on” of the fluorescence signal. Specifically, we suggest that intramolecular charge transfer between the OH oxygen atom lone pair electrons and the electron-deficient europium ion is switched on, activating the emissive features of **DOTA-perox** (Scheme 2).

The optical properties of **DOTA-perox** in the presence of H_2O_2 were also monitored using UV absorbance and luminescence emission spectroscopies (Figures S17A and S17B). The emission maximum at 620 nm steadily increased as a function of the H_2O_2 concentration (Figure S17C). The time required to reach saturation in terms of the luminescence intensity gradually decreased with increasing H_2O_2 concentration. This is ascribed to increasing H_2O_2 concentrations serving to accelerate the reduction of **DOTA-perox** to give activated **DOTA-perox**. In most cases, saturation was reached within approximately 20 min. The detection limit was calculated to be 58.3 ng/mL H_2O_2 (Figure S17D). The probe was exposed to 200 μM H_2O_2 at 37 °C for 30 min to verify that it was H_2O_2 that was mediating the

activation of **DOTA-perox.** Only one significant peak, corresponding to the activated probe, was observed by HRMS analysis ([M + H] = 630.110) (Figure S18).

Mirroring what was done for **BODIPY-perox**, before testing the ability of probe **DOTA-perox** to signal the presence of H_2O_2 in a cellular model system, we examined whether interference was seen in the presence of other biologically relevant analytes, including thiol amino acids (cystine, homocysteine and glutathione) biologically relevant metal ions (K^+, Mg^{2+}, Ca^{2+}, Zn^{2+}), redox-active species (ascorbic acid, vitamin B_6, HSA, H_2O_2, and glucose), enzymes (lipase, pepsin, trypsin, and phosphatase), thiol amino acids (cysteine and glutathione) and non-thiol amino acids (alanine, serine, lysine, arginine, and glutamic acid). We observed no spectroscopic changes in the presence of these potentially interfering analytes (Figure S19A). The fluorescence intensity of **DOTA-perox** in the presence and absence of H_2O_2 was then monitored as a function of pH and time at λ_{em} =615 nm (Figures S19B-D). The time required to reach fluorescence saturation gradually decreased as a function of increasing H_2O_2. In the case of the enzyme studies, an increase in the enzyme concentration also accelerated the reduction. **BODIPY-perox** was also subjected to various important oxidizing agents, including peroxyacetic acid (CH_3CO_3H), hypochlorite (ClO^-), singlet oxygen ($^1O_2$), superoxide (O_2^-), and peroxynitrile ($ONOO^-$), at a concentration of 200 μM for each of these potential interferants. The fluorescence intensity did not notably increase in response to these additional substances (Figures S20). Notably, **BODIPY-perox** exhibited a weaker response to $ONOO^-$ compared to H_2O_2. We also carried out tests with lipid droplet analogs, such as phosphatidylserine (PC), phosphatidylethanolamine (PE), phosphatidylglycerol (PG), phosphatidylserine (PS), and phosphatidylinositol (PI) (Figure S21). The results revealed that the presence of other lipid droplet analog substances did not significantly increase the fluorescence intensity. Both probes, **DOTA-perox** and **BODIPY-perox**, demonstrated favorable plasma stability over a 72-hour period (Figure S22). Photostability was also observed throughout the observation period (Figure S23). Taken in concert, these findings provide support for the suggestion that **BODIPY-perox** will exhibit selectivity for H_2O_2 in complex biological environments.

3.3. CEST MRI analysis of the activated probes in solution

As a complement to the above studies, we investigated whether probe activation could be monitored using CEST MRI. The reduced probes possess a phenolic OH group capable of proton exchange with the surrounding water. We thus expected that saturation of these protons with a radio frequency (RF) pulse would increase the CEST MRI signal owing to a decrease in the water signal (cf. Scheme 3). Because the CEST signal was expected to be pH-dependent, we initially examined the CEST MTR_{asym} (%) (Fig. 4A), Z-spectra (Fig. 4B), and MTR_{asym} (%) color map (Fig. 4C) of 5 mM aqueous **BODIPY-perox** solutions at pH values ranging from 5 to 8 in the presence of H_2O_2 (1 mM).

BODIPY-perox exhibited a broad CEST spectrum of 0.5–12 ppm, with a peak of approximately 6 ppm. Subsequent CEST imaging confirmed that the probe **BODIPY-perox** could be used to monitor H_2O_2 activity over a wide range of pH values using MRI. As seen in a previous study, the CEST signal produced by activated **BODIPY-perox** and ascribed to the OH protons proved pH-sensitive [43]. MTR_{asym} (%) spectra for different saturation

field strengths (B_1) from 1 to 6 μT for solutions at pH = 6.5 are presented in Fig. 4D. MTR_{asym} (%) values (Fig. 4E) and MTR_{asym} (%) CEST color map (Fig. 4F) at 6 ppm increased with saturation power from 1 to 5 μT, eventually saturating at 6 μT. We then selected B_1 =4.8 μT for all subsequent experiments, as it provided a comparable CEST signal at ~6 ppm to that at the higher B_1 value but with a narrower spectrum. We assessed the concentration dependence of the CEST spectra under slightly acidic conditions (pH = 6.5), considering that malignant tumors are often acidic [44]. The 6 ppm peak from the phenolic OH group could be observed in the CEST Z-spectra (Fig. 4G) and is reflected in the MTR_{asym} (%) values (Fig. 4H). Even at the lowest concentration of **BODIPY-perox** (0.5 mM), the MTR_{asym} (%) peaks were greater than 10%, making them easily detectable. The corresponding CEST images at 6 ppm demonstrated readily discernible CEST signal changes as a function of **BODIPY-perox** concentration. Additionally, we performed CEST experiments with **DOTA-perox** and observed behavior similar to that seen for **BODIPY-perox** as reflected in the corresponding Z-spectra (Figure S24A), MTR_{asym} (%) spectra (Figure S24B), and MTR_{asym} (%) color maps (Figure S24C).

3.4. In vitro activation of probes and imaging of HeLa cells

Before conducting fluorescence imaging of HeLa cells, we assessed the biocompatibility of both **DOTA-perox** and **BODIPY-perox** against normal cells (NIH3T3, WI38, HEK293, and BMMC), as well as cancer cells (HepG2, U87MG, A549, HeLa, and MDA-MB-231) at concentrations ranging from 0 to 20 mM for 24 h. No appreciable cytotoxicity was observed (Figure S25). On this basis we considered it likely that these probes would possess sufficient biocompatibility to allow for their use in H_2O_2 detection. Flow cytometric analysis of **BODIPY-perox** (5 μM) revealed 3.2–4.8 times higher H_2O_2 levels in cancer cell lines than normal cells (Figure S26A). In contrast, only a 1.3–2.0-fold difference in H_2O_2 levels in cancer cells compared to normal cells was seen for **DOTA-perox** (5 μM) (Figure S26B). Given its lower H_2O_2 sensitivity, **DOTA-perox** was not used for further studies. In contrast, an effort was made to analyze the features of **BODIPY-perox** in detail. Further evidence supporting selective cancer cell imaging with HeLa cells as compared to normal cells ((NIH3T3, WI38, and HEK293), was obtained through confocal scanning laser microscopy (CLSM) imaging studies. These investigations revealed that **BODIPY-perox** produces a statistically significant level of fluorescence increase under simulated oxidative conditions (Figure S27).

We investigated the cellular uptake of **BODIPY-perox** and its intracellular response to endogenous H_2O_2 by CLSM. After incubation with 4 μM **BODIPY-perox** for 15 min, a faint red fluorescence inside HeLa cells was observed. The fluorescence intensity increased when the HeLa cells were pretreated with 50 μM H_2O_2 for 30 min, followed by **BODIPY-perox** treatment for 15 min (Fig. 5A). The relative mean fluorescence intensity (MFI) was enhanced approximately two-fold when the cells were pretreated with H_2O_2 (Fig. 5B). The observed increase in MFI is ascribed to the elevated endogenous H_2O_2 levels. The H_2O_2 serves to reduce catalytically **BODIPY-perox**, resulting in an increase in the fluorescence intensity. Further evidence of selective H_2O_2-reduced cell imaging was provided by fluorescence-activated cell sorting (FACS) analysis of HeLa cells (Fig.

5C). HeLa cells pretreated with H_2O_2 (50 μM) exhibited approximately 1.5 times brighter fluorescence than the probe-treated cells alone.

To evaluate the efficacy of **BODIPY-perox** to map H_2O_2 levels in a tumor microenvironment, we performed fluorescence microscopy imaging of HeLa cancer cells cultured in 3D spheroids (Fig. 5D and E). After incubation with **BODIPY-perox** at concentrations of 10 or 20 μM for 30 min, the MFI increased at both concentrations under tumor microenvironment conditions as determined relative to the non-treated group. We then recorded the MTR_{asym} (%) curves for HeLa cells in the presence or absence of the probe **BODIPY-perox** (0, 0.5, and 1 mM). The CEST spectra (Fig. 5F) contained a main peak at a maximum of ~2.5 ppm, which increased with **BODIPY-perox** concentration. The CEST color map generated at 2.5 ppm showed distinctly enhanced CEST contrast with increasing **BODIPY-perox** concentration. Based on CEST experiments involving independent HeLa cells at different concentrations of **BODIPY-perox**, the signal intensity in HeLa cells containing the probe (0, 0.5, and 1 mM; n = 3 each) was statistically distinct from that in the non-treated cells under identical conditions (Fig. 5H). These results support the core contention of this study, namely, that **BODIPY-perox** can be used to map H_2O_2 levels in cancer cells and thus serve as a probe that may have a role to play in assessing malignancy.

We also tested the ability of **BODIPY-perox** to detect endogenous H_2O_2 in HeLa cells generated by lipopolysaccharide (LPS) treatment, which is known to generate reactive oxygen species as the result of H_2O_2 production [34]. In this study HeLa cells were incubated with 100 nM/mL LPS for 24, 48, or 72 h and then treated with probe **BODIPY-perox** (0.5 μM) for 15 min and washed and imaged (Fig. 6A). FACS analysis showed a clear increase in fluorescence intensity in the LPS-stimulated HeLa cells compared to the control cells (Fig. 6B). Additionally, the fluorescence signal increased proportionally with the LPS treatment time reflecting the expectation that longer incubation with LPS would produce higher levels H_2O_2 in the HeLa cells. The production of H_2O_2 by LPS treatment was monitored by CLSM. As shown in Fig. 6C, the fluorescence intensity increased with LPS treatment time (24, 48, and 72 h) after incubation with **BODIPY-perox** (0.5 μM). In contrast, we observed a relatively weak fluorescence in the LPS non-treated group. The MFI increased by approximately 1.5-fold after treating with LPS for 24 h. An approximately 2.1-fold increase was seen after 48 h, and an approximately 3-fold increase was seen after 72 h as compared to the untreated group (Fig. 6D).

Phorbol 12-myristate 13-acetate (PMA) generates H_2O_2 at the cellular level via superoxide [30,31]. HeLa cells treated with PMA (1 μg/mL) for 60 min exhibited higher **BODIPY-perox** fluorescence than control cells as determined by CLSM (Figure S29). Moreover, adding DPI as a broad-spectrum inhibitor or ebselen as a general antioxidant quencher of H_2O_2 inhibited the H_2O_2-induced enhancement of the **BODIPY-perox** fluorescence (Figure S29). As noted above, the cellular H_2O_2 levels could be changed by subjecting to LPS treatment (100 nM/mL). Further support for this conclusion came from western blot analyses of two recognized apoptosis proteins (BCL2 and Bax) (Fig. 6E). Increased production of H_2O_2 during LPS treatment results in the activation of apoptosis, increased Bax protein expression, and decreased BCL2 expression. Bax protein expression increased

by approximately 4.5-fold after 72 h of LPS treatment, whereas BCL2 protein expression decreased by approximately 3.8-fold (Fig. 6F). Actin was used as a control.

3.5. In vivo and ex vivo imaging of HeLa cell tumor

To assess the potential of **BODIPY-perox** as a tumor-targeting H_2O_2-activatable fluorescence/MRI probe for bioimaging, we conducted experiments using a HeLa cell tumor xenograft mouse model. After establishing the tumor model, **BODIPY-perox** (5 mg/kg) was administered intravenously (IV) to the mice through their tail veins. CEST MR imaging with pre-saturation using an RF pulse (single hard pulse of B_1 = 3.6 μT, 1 s) was carried out using a 4.7 T animal MRI system (Biospec 47/40, Bruker) before and after the IV injection of **BODIPY-perox**. T_2-W, CEST, and merged images are displayed in panels A and B of Fig. 7, showing the state of the HeLa tumor xenograft mice before and 20 h after IV treatment with **BODIPY-perox**. After injection of this probe, we observed CEST signal enhancement at 2.5 ppm, primarily at the tumor sites (indicated by the yellow circle). This observed enhancement is thought to reflect the selective activation of the boronic ester group within **BODIPY-perox** at the tumor site. The MTR_{asym} (%) value at 2.5 ppm within the tumor region increased approximately 2.5-fold 20 h after the injection of **BODIPY-perox** (Fig. 7C and D). These findings are taken as evidence that the CEST signal was enhanced following probe injection and that tumor-derived H_2O_2 actively promotes the “switching-on” of probe **BODIPY-perox**.

Inspired by the CEST imaging results, we performed a time-dependent in vivo fluorescence imaging study of **BODIPY-pero**x at 730 nm in xenograft HeLa tumor models and other organs. This study was carried out using an optical imaging system (IVIS Spectrum, PerkinElmer). The tumor-bearing nude mice were IV injected with **BODIPY-perox**. Imaging was then carried out at various times. Enhanced fluorescence intensity was observed at the tumor site 6 h after injection, a finding interpreted in terms of the accumulation of activated **BODIPY-perox** at the tumor site (Fig. 8A). Quantitative analysis revealed that the fluorescence intensity in the **BODIPY-perox** group at the tumor site increased in a time dependent manner and consistently exceeded that of the background over the 6–48 h time window post-injection (Fig. 8B). At 24 h, for instance, the fluorescence intensity at the tumor site was 4-fold higher than background.

The positive results of the time-dependent fluorescence imaging encouraged us to perform complementary time-dependent CEST imaging. We recorded CEST images of mice before **BODIPY-perox** injection, which served as a control. We observed extensive CEST stimulation between 16 and 20 h after injection, a finding interpreted in terms of progressive activation of **BODIPY-perox** (Fig. 8C and D). The MTR_{asym} (%) values displayed a gradual and statistically significant 2.1-fold increase at the tumor site 20 h after injection (Fig. 8D). In line with the fluorescence data, these CEST results revealed a higher signal intensity at the tumor site 20 h after injection.

The biodistribution of **BODIPY-perox** was studied in mice bearing HeLa tumors 20 h after injection (Fig. 8E). Phosphate buffered saline (PBS) was used as a control. After sacrifice, selected organs and tumor tissues were harvested from the mice and used to compare their

respective fluorescence intensities. Solid tumors from animals treated with PBS showed no noticeable fluorescence, whereas obvious fluorescence was seen in the tumors and kidneys of mice treated with **BODIPY-perox**.

The strong signal observed in the mouse kidneys during these ex vivo experiments is attributed to the renal excretion of **BODIPY-perox**. We detected relatively weaker ex vivo fluorescence signals in the liver and none in the heart or spleen. Quantitative analysis revealed a 4.1-fold higher fluorescence intensity for **BODIPY-perox** relative to PBS in the tumor region (Fig. 8G). This increase was recapitulated in the tumors collected from two groups (**BODIPY-perox** or PBS-injected), where again a 4-fold increase in the fluorescence intensities for **BODIPY-perox** was seen relative to the PBS control (Fig. 8F and H). **BODIPY-perox** accumulation within the tumor is explained on the basis of the enhanced permeability and retention (EPR) effect [33,45–47]. Importantly, our probe, **BODIPY-perox**, exhibited no negative side effects during or after treatment. These results underscore the effectiveness of our approach to activate selectively probes (**BODIPY-perox** in the present instance) within tumors using H_2O_2 as a trigger. More specifically, our findings serve to confirm that tumors can be imaged effectively in vivo using the fluorescence/CEST signal emanating from activated **BODIPY-perox**.

4. Conclusions

In summary, we developed a highly sensitive and selective tumor-targeting probe, **BODIPY-perox**, that permits the noninvasive detection of intracellular hydrogen peroxide (H_2O_2) in cancer cells. This probe relies on the incorporation of a biocompatible NIR fluorophore BODIPY moiety into an H_2O_2-sensing boronic ester. Using a combination of flow cytometry, confocal microscopy, fluorescence imaging, and CEST MRI, we demonstrated that **BODIPY-perox** may be used to monitor accurately the variations in H_2O_2 levels produced by endogenous sources in various cell types and repeatative stimuli. The ability to monitor H_2O_2 levels in cells allows cancer cells to be distinguished effectively from normal cells. In vitro studies revealed that **BODIPY-perox** displays acceptable biocompatibility and that it may be used to distinguish cancer cells from normal cells. Follow-up in vivo tests using a xenograft mouse cancer model revealed that **BODIPY-perox** selectively accumulates in solid tumors and produces maximal fluorescence and CEST signal intensity roughly 48 h after injection. No adverse events or side effects were seen. We thus suggest that **BODIPY-perox** or analogous H_2O_2-sensitive probes could prove useful in the early detection and treatment of cancer.

Supplementary Material

Refer to Web version on PubMed Central for supplementary material.

Acknowledgments

This work was supported by the National Research Foundation of Korea (NRF) grant funded by the Korea government (MSIT) (KSH, 2020R1A2C2012011), and grants (KSH, A423100 and J-HC C320000) from Korea Basic Science Institute. The work in Austin was supported by the Robert A. Welch Foundation (F-0018 to JLS) and the National Cancer Institute (CA 68682 to JLS).

Biographies

Sanu Karan received his Ph.D. degree in Analytical Science from Chungnam National University, Korea, in 2022. Presently, he serves as a postdoctoral researcher at the Korea basic Science Institute in Cheongju, Korea. His research focuses on drug delivery and bio-imaging, as well as the development of endogeneous stimulated fluorescent probes.

Jee-Hyun Cho received her master's degree in physical chemistry (with a focus on NMR) from Seoul National University, Korea, and her Ph.D. in analytical chemistry (specializing in MRI) from Chung-Ang University, Korea. Her research is primarily centered on analyzing disease characteristics and advancing diagnostic techniques using MRI methodologies, including multiple quantum MRI, CEST MRI, and MR spectroscopy. Within her laboratory, she has access to state-of-the-art imaging equipments, including 7 T and 3 T human MRI, as well as a 9.4 T animal MRI scanner. Her research encompassess a wide range of studies involving diseases in various animal models, including mice, rats, monkeys, and humans.

Jonathan L. Sessler did his undergraduate work at the University of California before receiving his Ph.D. from Stanford University in 1982. He is presently the Doherty-Welch Chair in Chemistry at The University of Texas at Austin. His research interests include drug discovery, sensor design, anion recognition, critical elements, expanded porphyrins, and supramolecular chemistry. He has published more than 900 papers and is an inventor of record on over 80 issued U.S. patents. He is a member of a number of learned societies, including the U.S. National Academy of Sciences, the American Academy of Arts and Sciences, the European Academy of Science, and the Chinese Academy of Science (Foreign Member).

Kwan Soo Hong earned Ph.D. degree in the Department of Physics from Seoul National University, Korea, in 1998. Currently, he serves as the Director of the Ochang Institute of Biological and Environmental Science at the Korea Basic Science Institute, Korea. Additionally, he holds a professorial position in the Department of Chemistry at ChungAng University, Korea. His research focuses on bionano-materials, organic optical biosensors for theranostic applications, and drug delivery systems.

Data availability

Data will be made available on request.

References

[1]. Razgulin A, Ma N, Rao J, Strategies for in vivo imaging of enzyme activity: an overview and recent advances, Chem. Soc. Rev 40 (2011) 4186–4216. [PubMed: 21552609]

[2]. Sun Y, Ma X, Cheng K, Wu B, Duan J, Chen H, Bu L, Zhang R, Hu X, Deng Z, Xing L, Hong X, Cheng Z, Strained cyclooctyne as a molecular platform for construction of multimodal imaging probes, Angew. Chem. Int. Ed 54 (2015) 5981–5984.

[3]. Baker M, Whole–animal imaging: the whole picture, Nature 463 (2010) 977–979. [PubMed: 20164931]

[4]. Pysz MA, Gambhir SS, Willmann JK, Molecular imaging: current status and emerging strategies, Clin. Radiol 65 (2010) 500–516. [PubMed: 20541650]

[5]. Sim N, Parker D, Critical design issues in the targeted molecular imaging of cell surface receptors, Chem. Soc. Rev 44 (2015) 2122–2134. [PubMed: 25711408]

[6]. Wu M, Shu J, Multimodal molecular imaging: current status and future directions, contrast media mol, Imaging 2018 (2018) 1382183.

[7]. Ntziachristos V, Going deeper than microscopy: the optical imaging frontier in biology, Nat. Methods 7 (2010) 603–614. [PubMed: 20676081]

[8]. Huang J, Li J, Lyu Y, Miao Q, Pu K, Molecular optical probes for early diagnosis of drug-induced acute kidney injury, Nat. Mater 18 (2019) 1133–1143. [PubMed: 31133729]

[9]. Lin J, Gao D, Wang S, Lv G, Wang X, Lu G, Wang X, Lu C, Peng Y, Qiu L, Stimuli-responsive macrocyclization scaffold allows in situ self-assembly of radioactive tracers for positron emission tomography imaging of enzyme activity, J. Am. Chem. Soc 144 (2022) 7667–7675. [PubMed: 35452229]

[10]. Lv G, Sun X, Qiu L, Sun Y, Li K, Liu Q, Zhao Q, Qin S, Lin J, PET imaging of tumor PD-L 1 expression with a highly specific nonblocking single-domain antibody, J. Nucl. Med 61 (2020) 117–122. [PubMed: 31253743]

[11]. Chen P, Wang H, Wu H, Zou P, Wang C, Liu X, Pan Y, Liu Y, Liang G, Intracellular synthesis of hybrid Gallium-68 nanoparticle enhances microPET tumor, Anal. Chem 93 (2021) 6329–6334. [PubMed: 33848118]

[12]. Dong L, Qian J, Hai Z, Xu J, Du W, Zhong K, Liang G, Alkaline phosphatase-instructed self-assembly of Gadolinium nanofibers for enhanced T2-weighted magnetic resonance imaging of tumor, Anal. Chem 89 (2017) 6922–6925. [PubMed: 28627868]

[13]. Wang LV, Hu S, Photoacoustic tomography: in vivo imaging from organelles to organs, Science 335 (2012) 1458–1462. [PubMed: 22442475]

[14]. Wang Y, Hu X, Weng J, Li J, Fan Q, Zhang Y, Ye D, A photoacoustic probe for the imaging of tumor apoptosis by caspase-mediated macrocyclization and self-assembly, Angew. Chem. Int. Ed 58 (2019) 4886–4890.

[15]. Steinberg I, Huland DM, Vermesh O, Frostig HE, Tummers WS, Gambhir SS, Photoacoustic clinical imaging, Photoacoustics 14 (2019) 77–98. [PubMed: 31293884]

[16]. Attia ABE, Balasundaram G, Moothanchery M, Dinish US, Bi R, Ntziachristos V, Olivo M, Review of clinical photoacoustic Imaging: current and future trend, Photoacoustics 16 (2019) 100144. [PubMed: 31871888]

[17]. Louie A, Multimodality imaging probes: design and challenges, Chem. Rev 110 (2010) 3146–3195. [PubMed: 20225900]

[18]. Zhang Y, Jeon M, Rich LJ, Hong H, Geng J, Zhang Y, Shi S, Barnhart TE, Alexandridis P, Huizinga JD, Seshadri M, Cai W, Lovell JF, Non-invasive multimodal functional imaging of the intestine with frozen micellar naphthalocyanines, Nat. Nanotechnol 9 (2014) 631–638. [PubMed: 24997526]

[19]. Veal EA, Day AM, Morgan BA, Hydrogen peroxide sensing and signaling, Mol. Cell 26 (2007) 1–14. [PubMed: 17434122]

[20]. Fruehauf JP, Meyskens JFL, Reactive oxygen species: a breath of life or death? Clin. Cancer Res 13 (2007) 789–794. [PubMed: 17289868]

[21]. Schoenfeld JD, Sibenaller ZA, Mapuskar KA, Wagner BA, Cramer-Morales KL, Furqan M, Allen BG, O_2- and H_2O_2-mediated disruption of Fe metabolism causes the differential susceptibility of NSCLC and GBM cancer cells to pharmacological ascorbate, Cancer Cell 31 (2017) 487–500. [PubMed: 28366679]

[22]. Poole LB, Nelson KJ, Discovering mechanisms of signaling-mediated cysteine oxidation, Curr. Opin. Chem. Biol 12 (2008) 18–24. [PubMed: 18282483]

[23]. Volpp BD, Nauseef WM, Clark RA, Two cytosolic neutrophil oxidase components absent in autosomal chronic granulomatous disease, Science 242 (1988) 1295–1297. [PubMed: 2848318]

[24]. Dinauer MC, Orkin SH, Brown R, Jesaitis AJ, Parkos CA, The glycoprotein encoded by the X-linked chronic granulomatous disease locus is a component of the neutrophil cytochrome b complex, Nature 327 (1987) 717–720. [PubMed: 3600768]

[25]. Balaban RS, Nemoto S, Finkel T, Mitochondria, oxidants, Aging Cell 120 (2005) 483–495.

[26]. Mattson MP, Pathways towards and away from alzheimer's disease, Nature 430 (2004) 631–639. [PubMed: 15295589]

[27]. Pop-Busui R, Sima A, Stevens M, Diabetic neuropathy and oxidative stress, Diabetes/Metab. Res. Rev 22 (2006) 257–273.

[28]. Ishikawa K, Takenaga K, Akimoto M, Koshikawa N, Yamaguchi A, Imanishi H, Nakada K, Honma Y, Hayashi J, ROS-generating mitochondrial DNA mutations can regulate tumor cell metastasis, Science 320 (2008) 661–664. [PubMed: 18388260]

[29]. Pierre VC, Allen MJ, Caravan P, Contrast agents for MRI: 30+ years and where are we going, J. Biol. Inorg. Chem 19 (2014) 127–131. [PubMed: 24414380]

[30]. Verwilst P, Park S, Yoon B, Kim JS, Recent advances in Gd-chelate based bimodal optical, MRI Contrast Agents 44 (2015) 1791–1806.

[31]. Forsen S, Hoffman RA, Study of moderately rapid chemical exchange reactions by means of nuclear magnetic double resonance, J. Chem. Phys 39 (1963) 2892.

[32]. Abo M, Urano Y, Hanaoka K, Terai T, Komatsu T, Nagano T, Development of a highly sensitive fluorescence probe for hydrogen peroxide, J. Am. Chem. Soc 133 (2011) 10629–10637. [PubMed: 21692459]

[33]. Chen Y, Shi X, Lu Z, Wang X, Wang ZA, A fluorescent probe for hydrogen peroxide in vivo based on the modulation of intramolecular charge transfer, Anal. Chem 89 (2017) 5278–5284. [PubMed: 28415838]

[34]. Iwashita H, Castillo E, Messina MS, Swanson RA, Chang CJ, A tandem activity-based sensing and labeling strategy enables imaging of transcellular hydrogen peroxide signaling, Proc. Natl. Acad. Sci. USA 118 (2021) e2018513118. [PubMed: 33622793]

[35]. Lippert AR, Keshari KR, Kurhanewicz J, Chang CJ, A hydrogen peroxide-responsive hyperpolarized 13C MRI contrast agent, J. Am. Chem. Soc 133 (2011) 3776–3779. [PubMed: 21366297]

[36]. Yu M, Beyers RJ, Gorden JD, Cross JN, Goldsmith CR, A magnetic resonance imaging contrast agent capable of detecting hydrogen peroxide, Inorg. Chem 51 (2012) 9153–9155. [PubMed: 22889331]

[37]. Park H, Chen J, Dimitrov IE, Park JM, Wang Q, Design and characterization of hyperpolarized 15N-BBCP as a H2O2-sensing probe, ACS Sens. 7 (2022) 2928–2933. [PubMed: 36255172]

[38]. Karan S, Cho MY, Lee H, Park HS, Han EH, Song Y, Lee Y, Kim M, Cho JH, Sessler JL, Hong KS, Hypoxia-responsive luminescent CEST MRI agent for in vitro and in vivo tumor detection and imaging, J. Med. Chem 65 (2022) 7106–7117. [PubMed: 35580357]

[39]. Ratnakar SJ, Viswanathan S, Kovacs Z, Jindal AK, Green KN, Sherry AD, Europium (III) DOTA-tetraamide complexes as redox-active MRI sensor, J. Am. Chem. Soc 134 (2012) 5798–5800. [PubMed: 22420507]

[40]. Karan S, Cho MY, Lee H, Lee H, Park HS, Sundararajan M, Sessler JS, Hong KS, Near-infrared fluorescent probe activated by nitroreductase for in vitro and in vivo hypoxic tumor detection, J. Med. Chem 64 (2021) 2971–2981. [PubMed: 33711229]

[41]. Zhu C, Falck JR, Transition metal-free ipso-functionalization of arylboronic acids and derivatives, Adv. Synth. Catal 356 (2014) 2395–2410. [PubMed: 25414624]

[42]. Liu H, Jablonska A, Li Y, Cao S, Liu D, Chen H, Van Ziji PCM, Bulte JWM, Janowski M, Walczak P, Liu G, Label-free CEST MRI detection of citicoline-liposome drug delivery in ischemic stroke, Theranostics 6 (2016) 1588–1600. [PubMed: 27446492]

[43]. Yang X, Jiang X, Wang W, Yang Q, Ma Y, Wang K, Catalyst-and solvent-free ipso-hydroxylation of arylboronic acids to phenols, RSC Adv. 9 (2019) 34529–34534. [PubMed: 35529971]

[44]. Estrella V, Chen T, Lloyd M, Wojtkowiak J, Cornnell HH, Ibrahim-Hashim A, Bailey K, Balagurunathan Y, Rothberg JM, Sloane BF, Johnson J, Acidity generated by the tumor microenvironment drives local invasion, Cancer Res. 73 (2013) 1524–1535. [PubMed: 23288510]

[45]. Dai H, Shen Q, Shao J, Wang W, Gao F, Dong X, Small molecular NIR-II fluorophores for cancer phototheranostics, Innovation 2 (2021) 100082. [PubMed: 34557737]

[46]. Kang H, Rho S, Stiles WR, Hu S, Baek Y, Hwang DW, Kashiwagi S, Kim MS, Choi HS, Size-dependent EPR effect of polymeric nanoparticles on tumor targeting, Adv. Healthc. Mater 9 (2020) 1901223.

[47]. Ye S, Hu JJ, Zhao QA, Yang D, Fluorescent probes for in vitro and in vivo quantification of hydrogen peroxide, Chem. Sci 11 (2020) 11989–11997. [PubMed: 34094420]

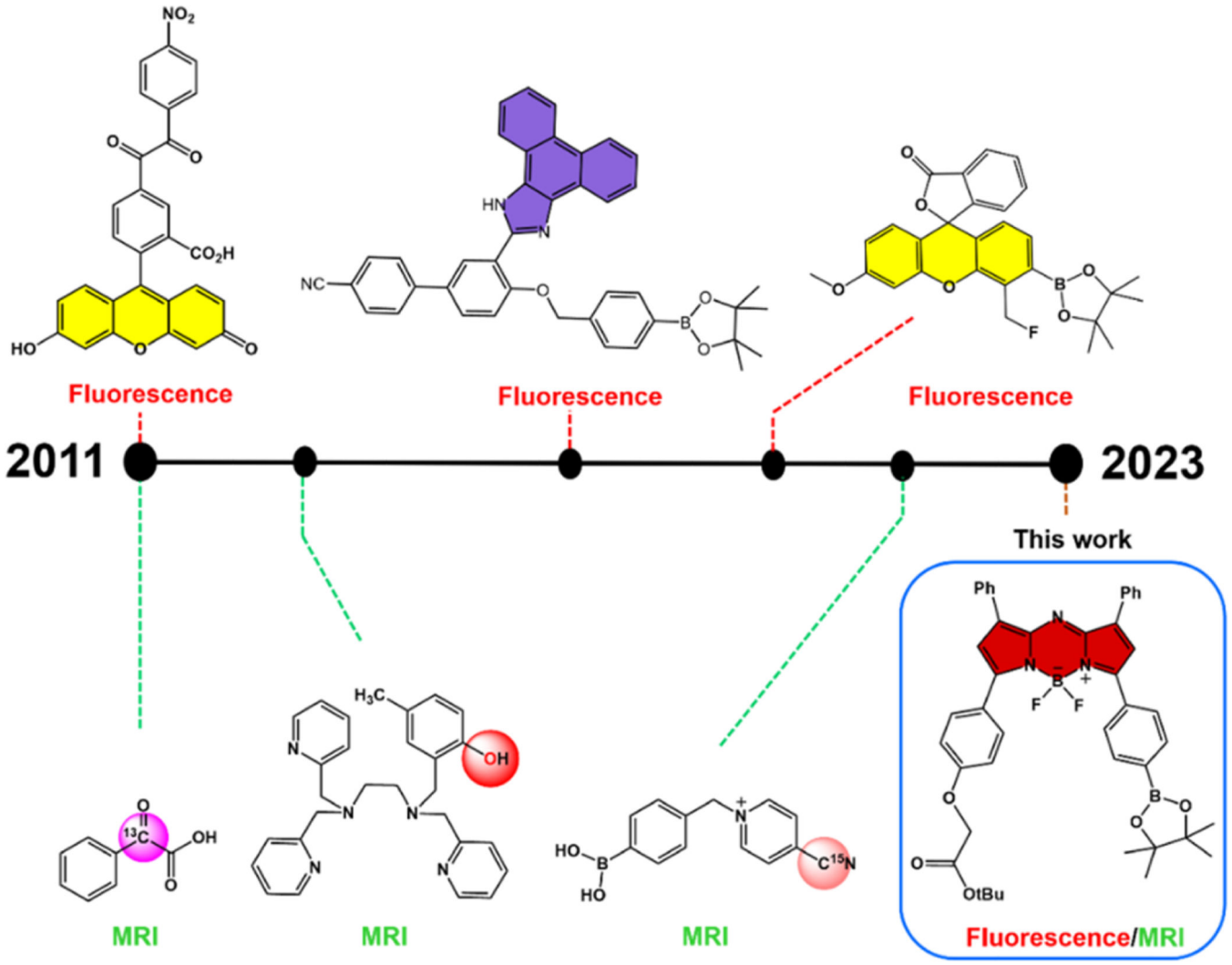

Fig. 1.

Timeline showing the development of small molecule H_2O_2-activatable probes and associated imaging modalities.

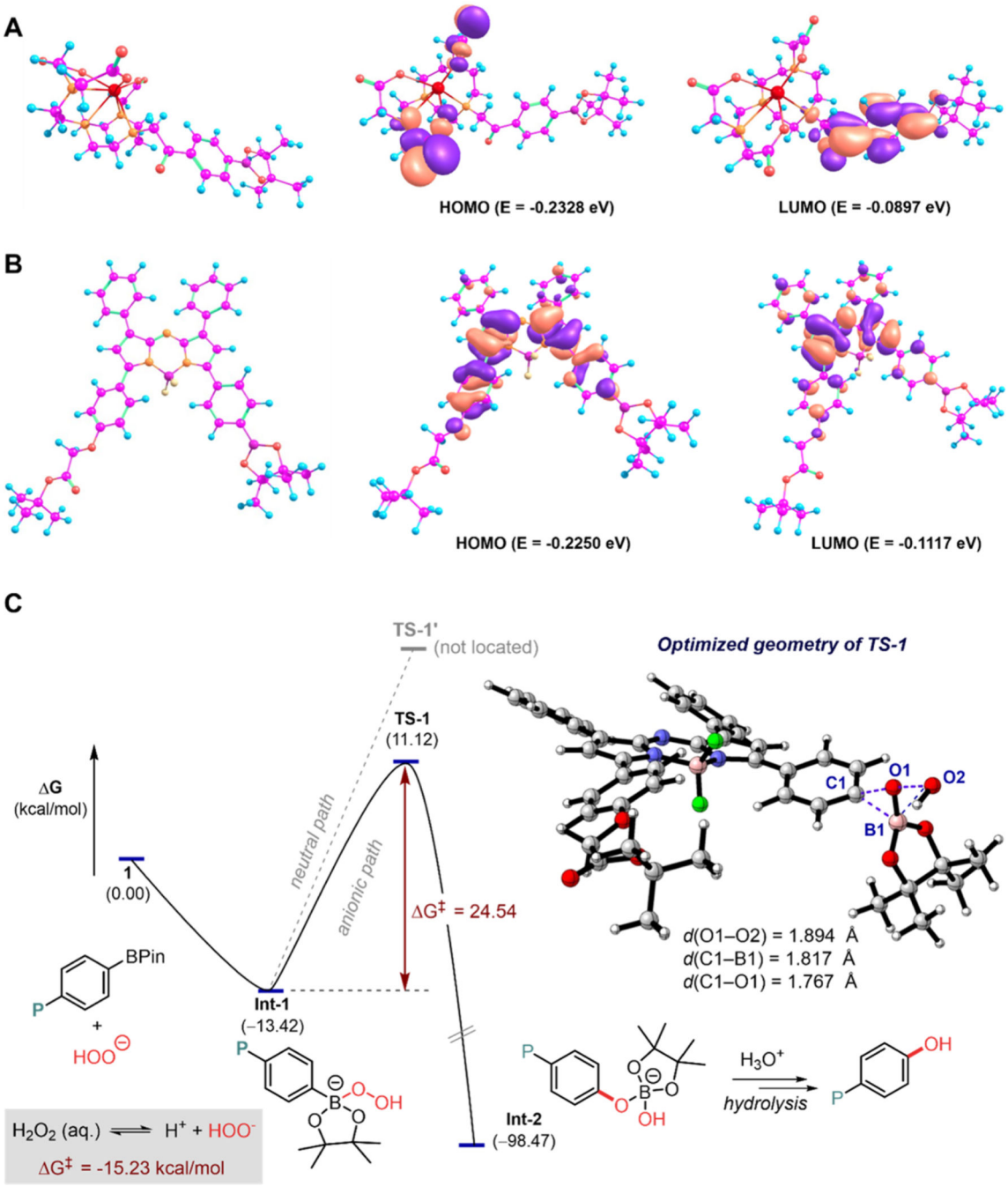

Fig. 2.

DFT-optimized structures and computed HOMO/LUMO gaps for **DOTA-perox** (A) and **BODIPY-perox** (B). The calculated energy gap for **DOTA-perox** is $\Delta E_{\text{DOTA-perox}}$ = (HOMO–LUMO) = −0.143 eV, while that for the **BODIPY-perox** is − 0.113 eV. (C) DFT-computed schematic energy diagrams and corresponding optimized geometries for intermediates proposed to be involved in probe cleavage. P = probe.

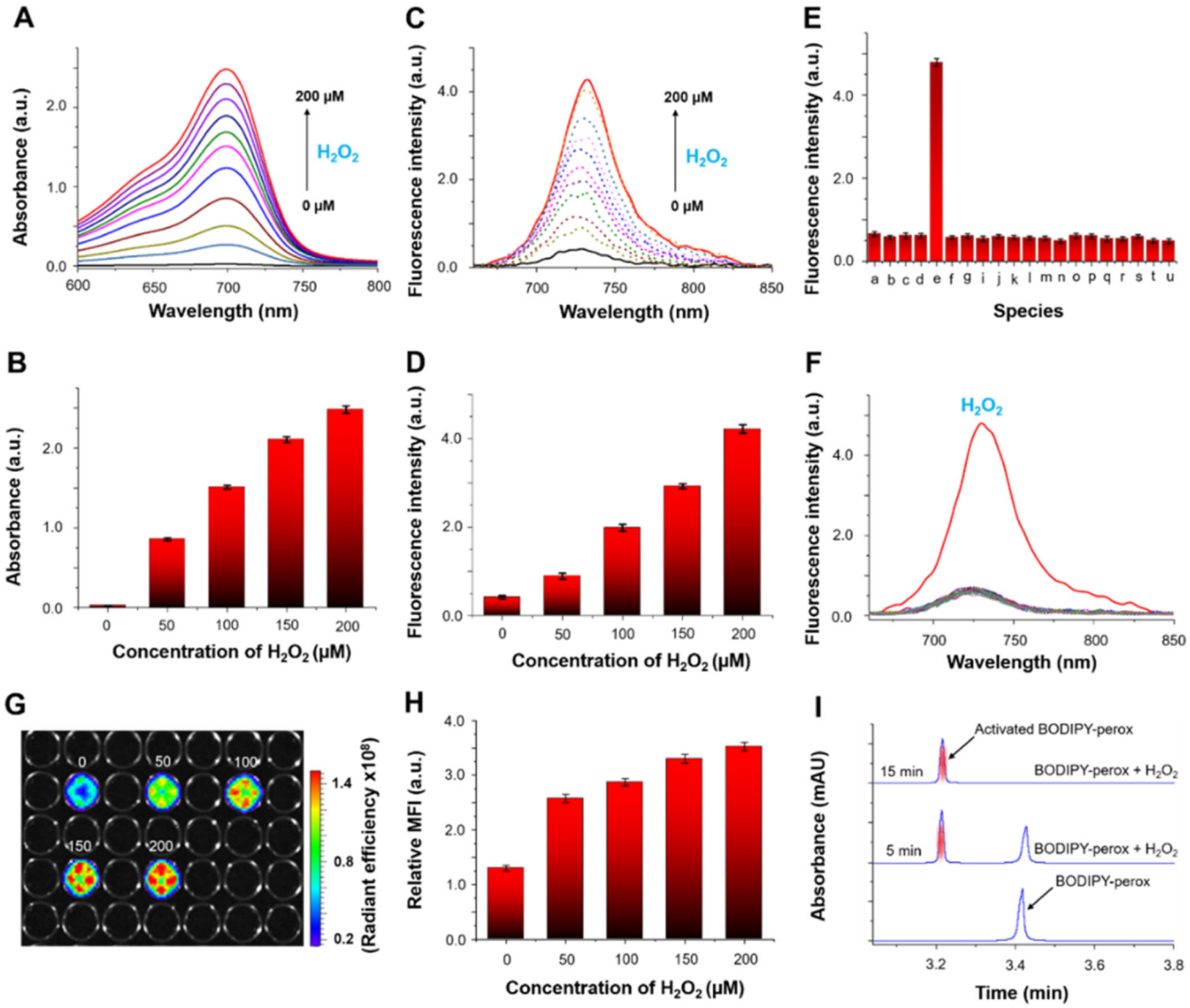

Fig. 3. Photophysical properties of BODIPY-perox before and after H_2O_2 treatment.

(A) UV absorption spectra of **BODIPY-perox** (5 μM) recorded in the presence of various H_2O_2 concentrations (0–200 μM). Fluorescence absorption (B) and emission (C) spectra (λ_{ex} = 685 nm) of **BODIPY-perox** recorded in the presence of different H_2O_2 concentrations (0, 50, 100 and 200 μM). (D) Emission intensity of **BODIPY-perox** (5 μM) recorded at various H_2O_2 concentrations (pre-incubated for 15 min at 37 °C) ($\lambda_{ex}/\lambda_{em}$ = 685/730 nm for all experiments, unless noted otherwise). (E) Fluorescence response of the **BODIPY-perox** probe (5 μM) to different potential interferants in blood serum: (a) blank (probe in PBS), and serum containing: (b) 150 mM KCl, (c) 2.5 mM $MgCl_2$, (d) 2.5 mM $CaCl_2$, (e) 200 μM H_2O_2, (f) 1 mM vitamin C, (g) 1 mM vitamin B_6, (h) 100 μM HSA, (i) 10 mM glucose, (j) 200 U/L lipase, (k) 100 μg/L pepsin, (l) 200 ng/mL trypsin (m) 200 U/L phosphatase, (n) 1 mM arginine, (o) 1 mM serine, (p) 5 mM glutathione, (q) 1 mM cysteine, (r) 1 mM lysine, (s) 1 mM glutamic acid, (t)) 1 mM tyrosine, (u)) 1 mM histidine. (F) Fluorescence response of **BODIPY-perox** (5 μM; at λ_{em} = 730 nm)

to different species present in blood serum (graphically). (G) Change in the fluorescence intensity of **BODIPY-perox** seen in response to treatment with various H_2O_2 concentrations (0, 50, 100, 150, and 200 μM) as measured using an optical imaging system (IVIS Spectrum, PerkinElmer) and (H) corresponding quantitative comparison of the fluorescence intensity with H_2O_2 concentration. (I) HPLC profiles of **BODIPY-perox** (5 μM) in the presence of H_2O_2 (200 μM) as determined a different indicated time. The data are the average of four independent experiments; the error bars represent standard deviations.

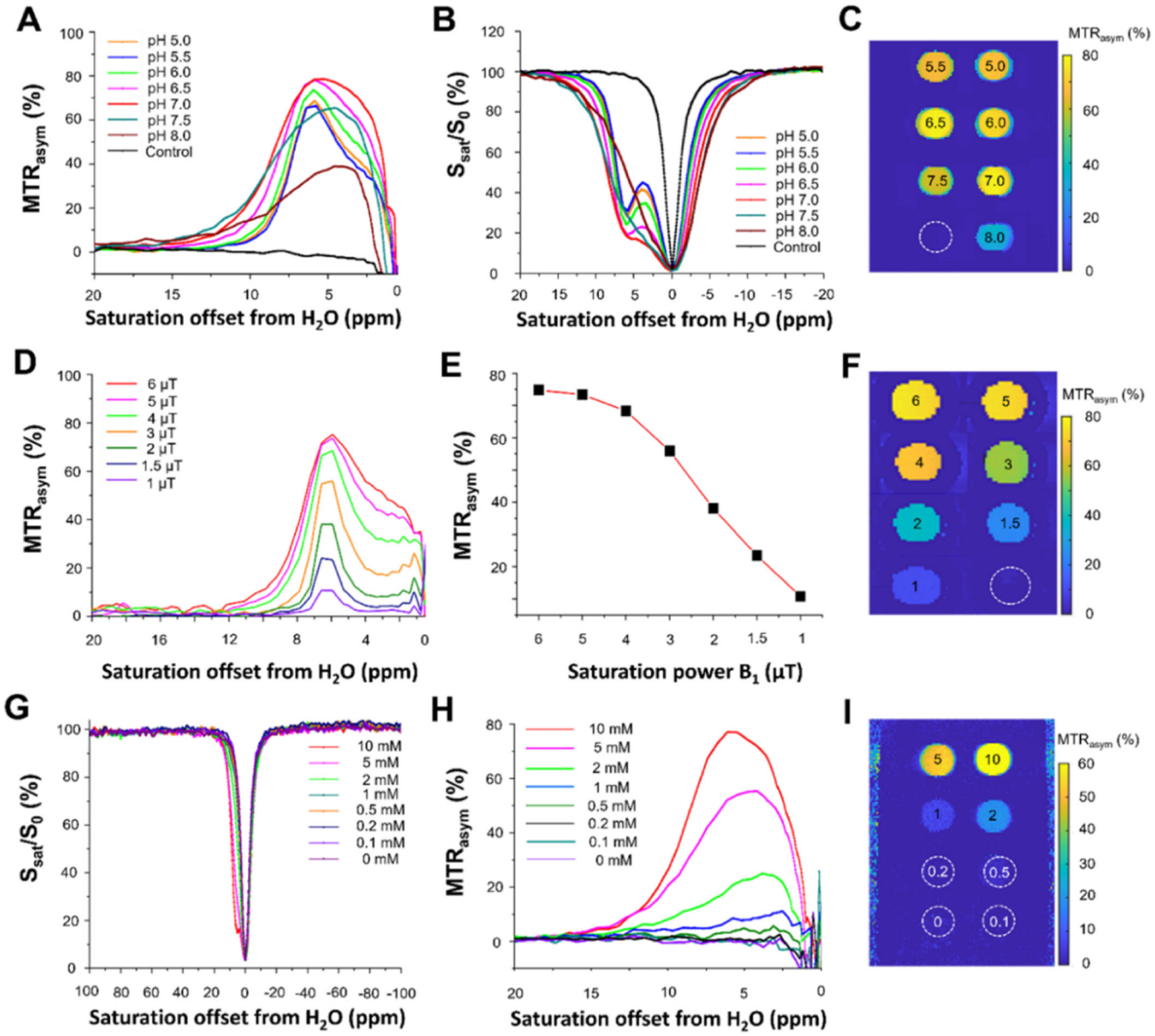

Fig. 4.

CEST signals produced by activated **BODIPY-perox**. (A) Calculated MTR_{asym} (%) values of aqueous 10 mM **BODIPY-perox** solutions at different pH values, (B) Z-spectra, and (C) representative MTR_{asym} (%) CEST color map at 6 ppm. (D) Saturation power (B_1) dependence of the MTR_{asym} (%) spectra of **BODIPY-perox** observed at pH = 6.5. (E) Calibration curve relating the MTR_{asym} (%) value to the saturation power based on the spectra. (F) MTR_{asym} (%) CEST contrast color map at 6 ppm. (G) Z-spectra values for different **BODIPY-perox** concentrations at pH = 6.5. (H) MTR_{asym} (%) and (I) corresponding MTR_{asym} (%) CEST image at 6 ppm.

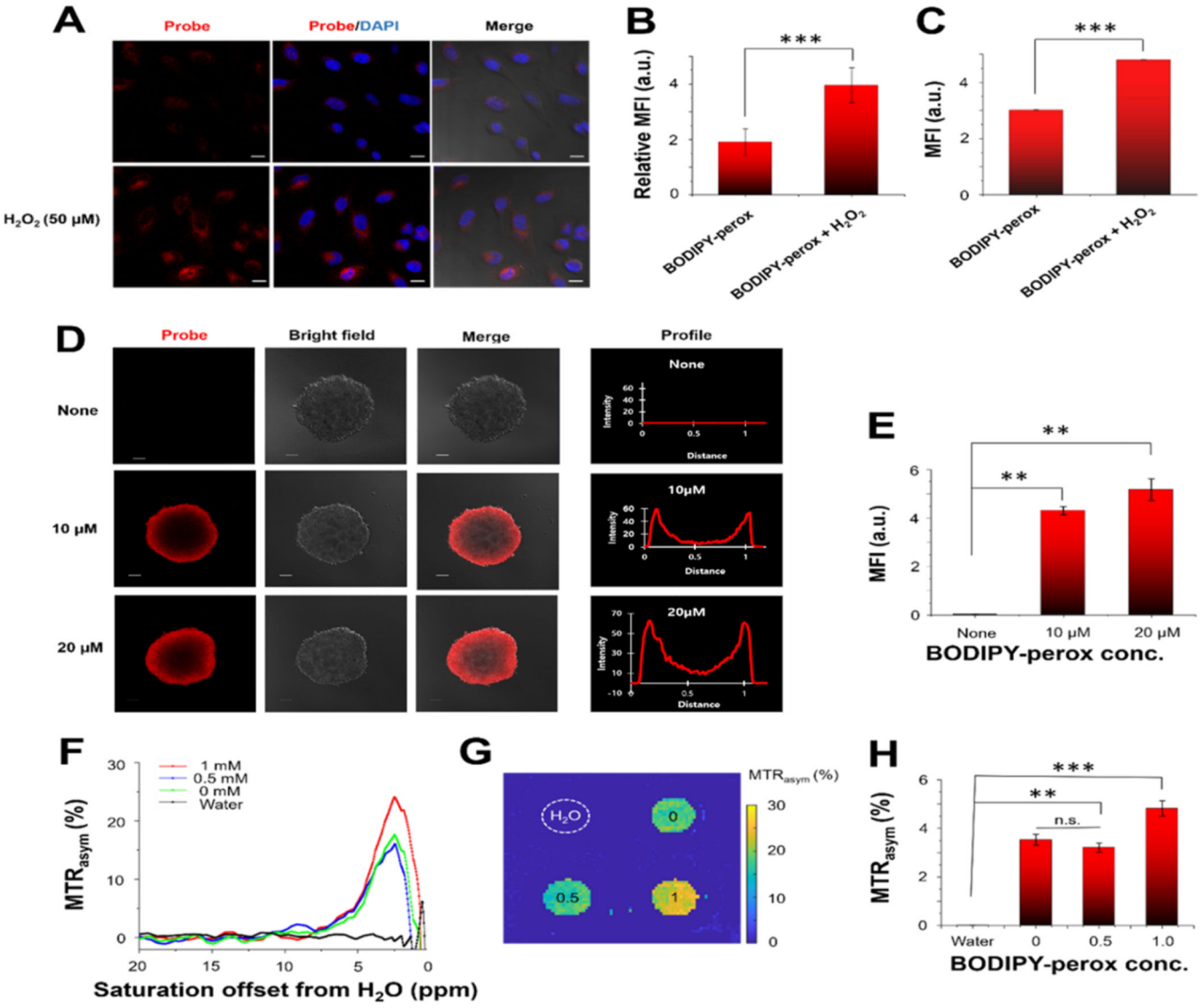

Fig. 5.

In vitro imaging of **BODIPY-perox** in HeLa cells. (A) Confocal laser scanning microscopy (CLSM) images of HeLa cells pre-treated with H_2O_2 or vehicle for 30 min, washed and incubated with **BODIPY-perox** (4 μM) for 15 min. Scale bars, 20 μm. (B) Corresponding quantitative comparison of fluorescence intensities measured from 15 individual cells using ImageJ (nonpaired Student's t-test). (C) Representative fluorescence-activated cell sorting (FACS) of HeLa cells pre-treated H_2O_2 (50 μM) for 30 min, washed with PBS three times, and incubated with **BODIPY-perox** for 15 min. (D) Fluorescence imaging of HeLa cell spheroids with **BODIPY-perox** (10 and 20 μM) for 30 min and (E) quantitative values of mean fluorescence intensity (MFI) of HeLa spheroids incubated with **BODIPY-perox**. Scale bars, 100 μm. (F) CEST spectrum of HeLa cells incubated in different concentrations of **BODIPY-perox** (0, 0.5, and 1 mM). (G) CEST contrast color map at 2.5 ppm and (H) corresponding statistical comparison of signal intensities determined from the color map. The data are averages of three experiments; error bars represent the standard deviations. p

values were determined using a nonpaired Student's t-test: n.s., nonsignificant; **, $p<0.01$; and ***, $p<0.001$.

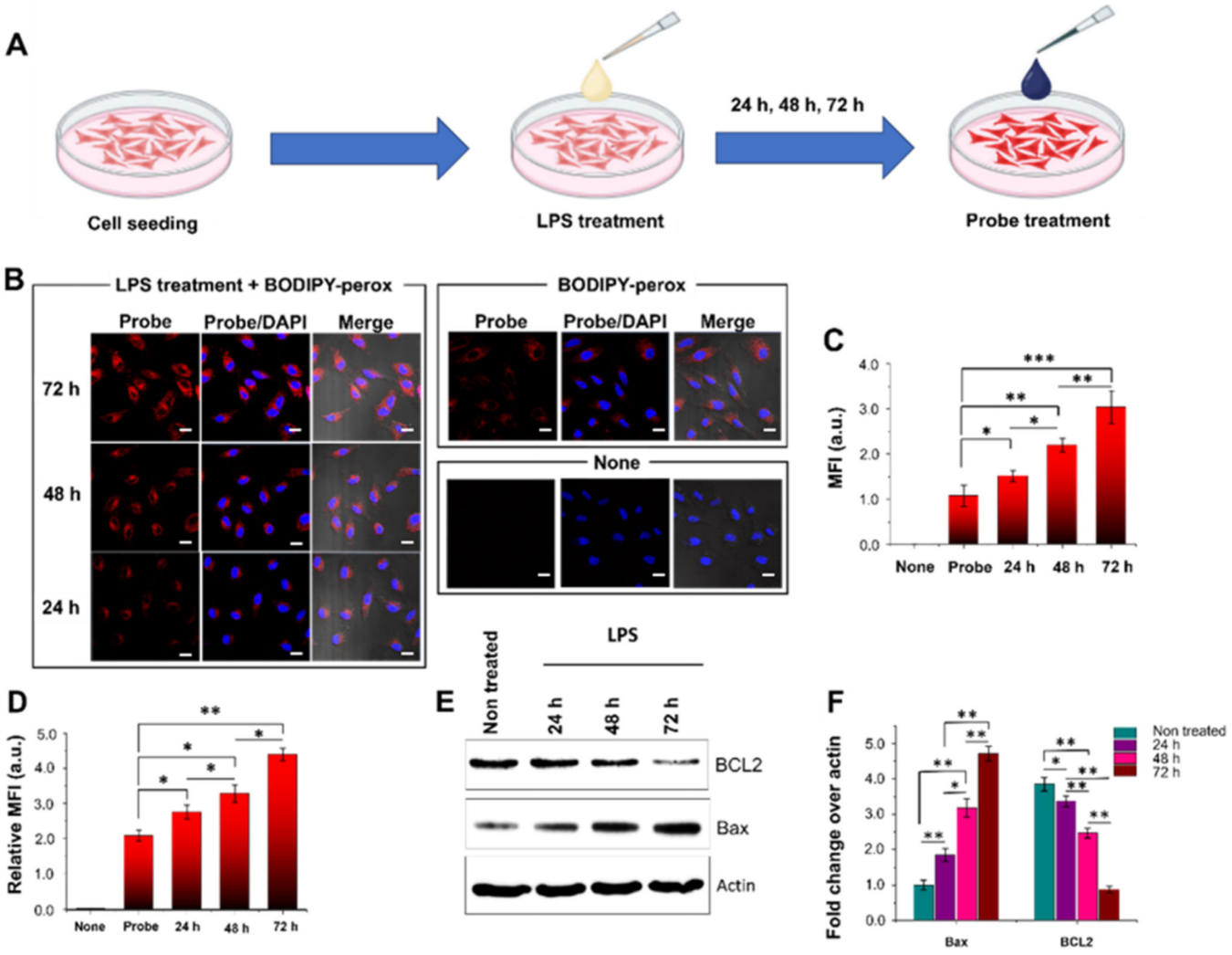

Fig. 6.

In vitro imaging of **BODIPY-perox** in HeLa cells treated with lipopolysaccharide (LPS). (A) Schematic showing the protocol used for LPS incubation with subsequent probe treatment. (B) CLSM images of HeLa cells pre-treated with LPS (100 ng/mL) or vehicle for 24, 48, and 72 h, prior to being incubated with **BODIPY-perox** (0.5 μM) for 15 min and washed and imaged. Scale bars, 20 μm. (C) Corresponding quantitative comparison of fluorescence intensities from 15 individual cells using the ImageJ software (nonpaired Student's *t* test). (D) FACS analyses of HeLa cells treated with LPS followed by **BODIPY-perox** for 24, 48, and 72 h. (E) Western blot analysis of reactive oxygen species (ROS)-related proteins (BCL2 and Bax) in HeLa cells treated with LPS or vehicle. β-Actin was used as a control. (F) Corresponding quantitative comparison of the BCL2 and Bax protein levels and β-actin control after LPS treatment.

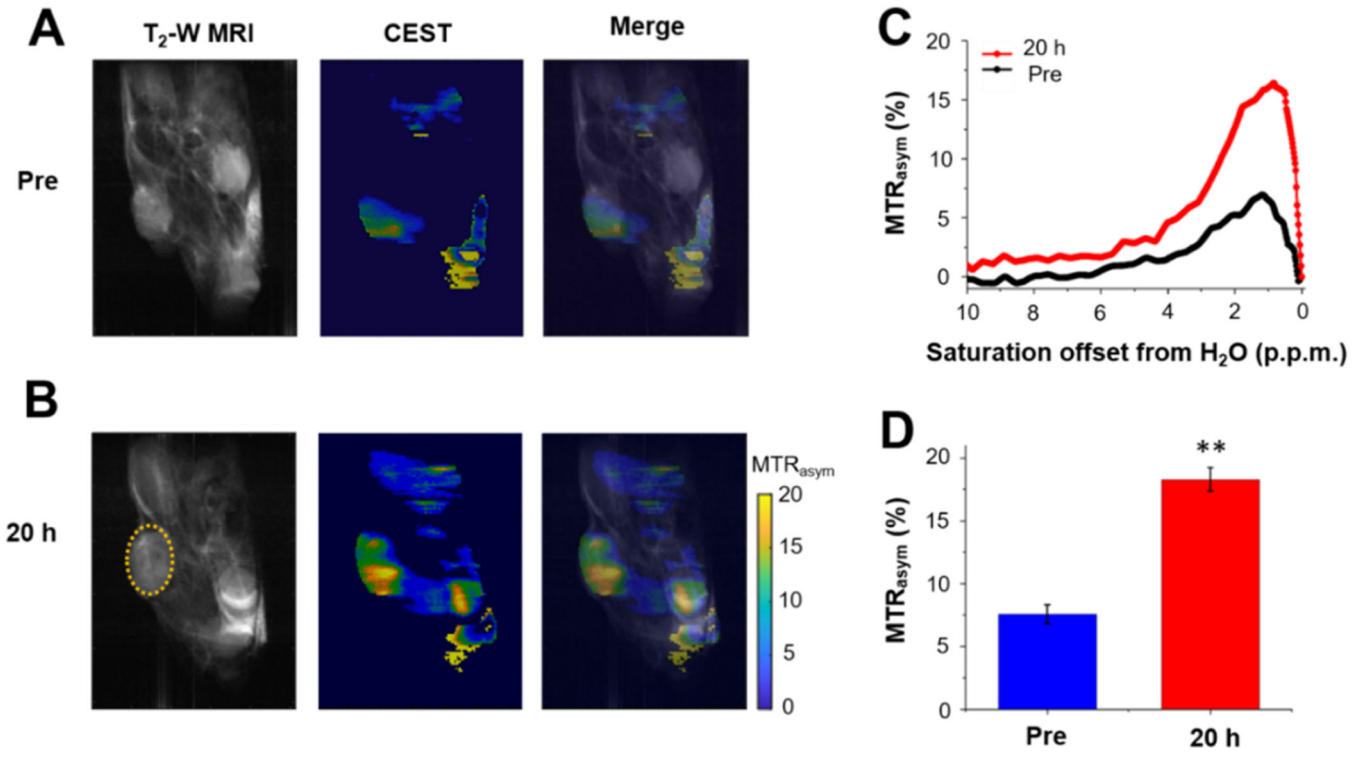

Fig. 7.

In vivo CEST imaging of **BODIPY-perox** in a HeLa xenograft mouse model. T_2-weighted (T_2-W) and CEST MR images obtained (A) before and (B) 20 h after intravenous (IV) injection of probe **BODIPY-perox** (5 mg/kg, 100 μL) into the HeLa tumor-bearing mice (n = 5). Each CEST MR image recorded at 6 ppm is merged with the corresponding T_2-W MR image. (C) MTR_{asym} value measured with saturation offset from water before and after injection of **BODIPY-perox** in the HeLa xenograft mouse model. (D) Quantitative comparison of the mean MTR_{asym} (%) values at 2.5 ppm for the tumor region (yellow dotted elipsoid). The data represent the average of four measurements with error bars showing the standard deviation. p values were determined using a nonpaired student's t test: **, $p<0.01$.

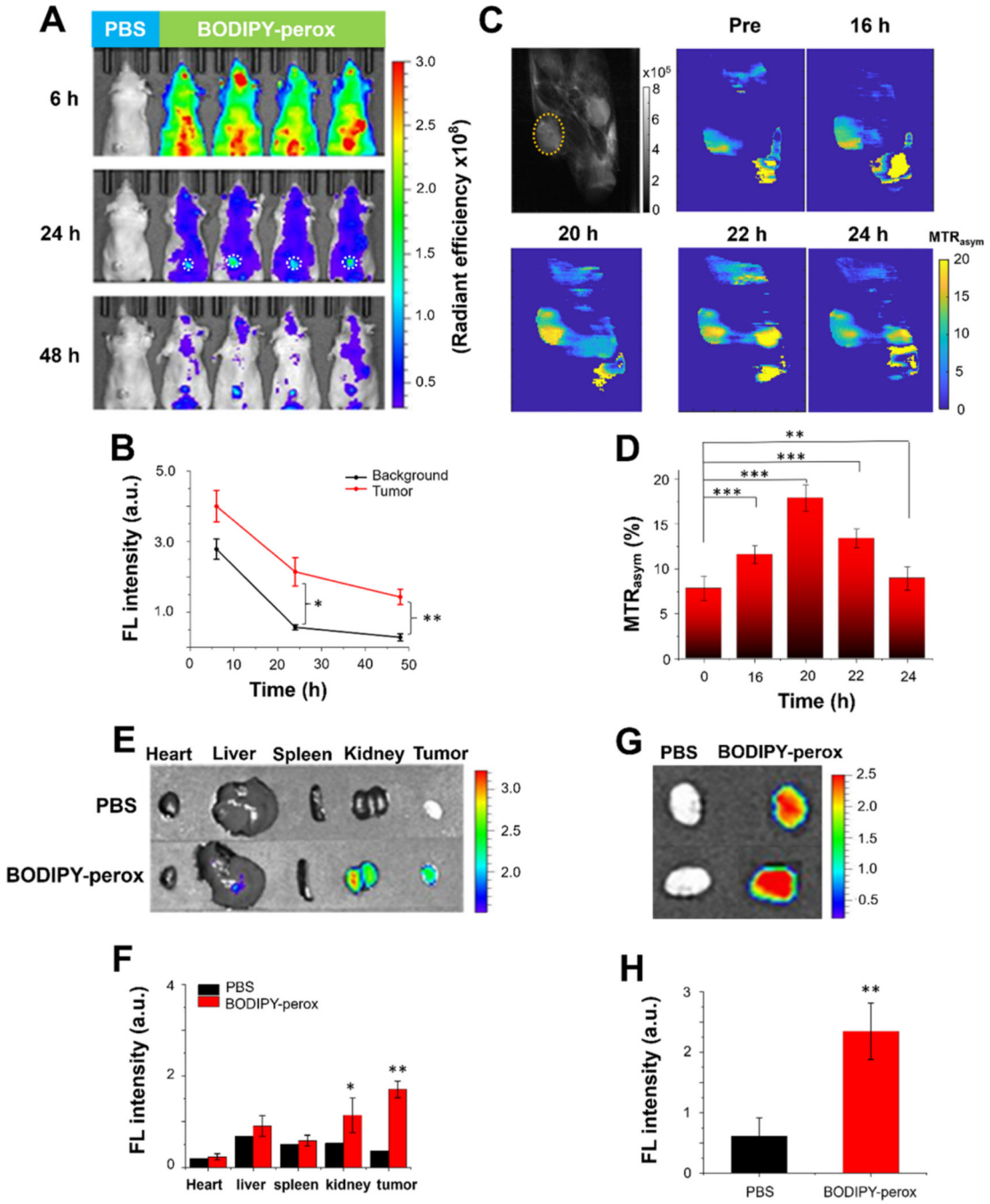

Fig. 8.

Dual imaging (fluorescence and CEST) in vivo tumor detection in a HeLa xenograft mouse model using **BODIPY-perox** as a probe. (A) Time-dependent in vivo optical imaging of xenograft HeLa tumor-bearing mice following intravenous (IV) injection of **BODIPY-perox** (5 mg/kg, 100 μL), and (B) corresponding quantitative comparison of fluorescence intensity obtained in the tumor region concerning body signal (background) ($n = 5$). (C) Complementary, time-dependent in vivo CEST imaging of probe **BODIPY-perox** in a HeLa xenograft mouse model. (D) Quantitative comparison of the MTR_{asym} (%) values at 2.5

ppm for the tumor region at different time points following injection of **BODIPY-perox** (nonpaired Student's t-test). (E) Representative ex vivo fluorescence images obtained from several organs, including the heart (1), liver (2), spleen (3), kidney (4), and tumor (5), extracted after the final in vivo imaging at 20 h, for the **BODIPY-perox** group compared to the PBS group. (F) Corresponding comparison of the fluorescence intensities measured in organs and tumors. (G) Ex vivo fluorescence images of tumor tissues (n = 5) and quantitative comparison (H) of fluorescence intensities for the **BODIPY-perox** and PBS groups. Error bars show standard deviations (nonpaired Student's t-test). *, $p<0.05$; **, $p<0.01$; and ***, $p<0.001$.

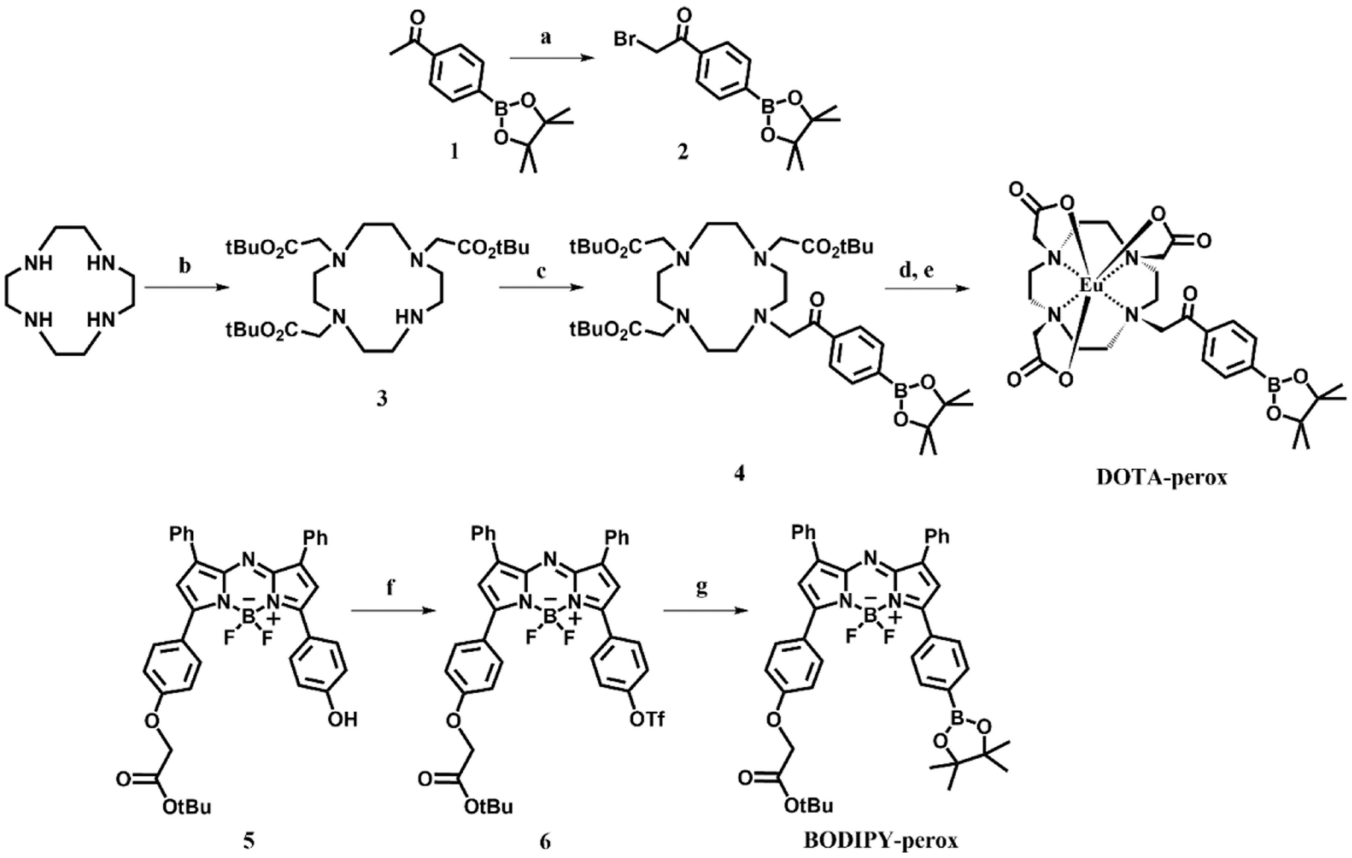

Scheme 1.

Synthesis of **DOTA-perox and BODIPY-perox. Reagents and reaction conditions: (a) Bromine in chloroform ($CHCl_3$) at room temperature (12** h); (b) *t-butyl bromoacetate, potassium carbonate (K_{2CO3}), dimethylformamide (DMF) at 75°C (18* h); (c) compound 2, K_{2CO3}, DMF at ~90°C (16 h); (d) trifluoroacetic acid (TFA) at room temperature (24 h); (e) europium(III) chloride hexahydrate ($EuCl_3 \cdot 6\ H2O$); (f) triflic anhydride (Tf2O), triethyl amine (Et3N), dichloromethane (DCM) at room temperature (12 h); (g) bis (pinacolato)diboron, [1,1´-bis(diphenylphosphine)ferrocene]dichloropalladium(II) ($PdCl_{2(dppf)}$, potassium acetate (KOAc), dimethylsulfoxide (DMSO), 80°C·

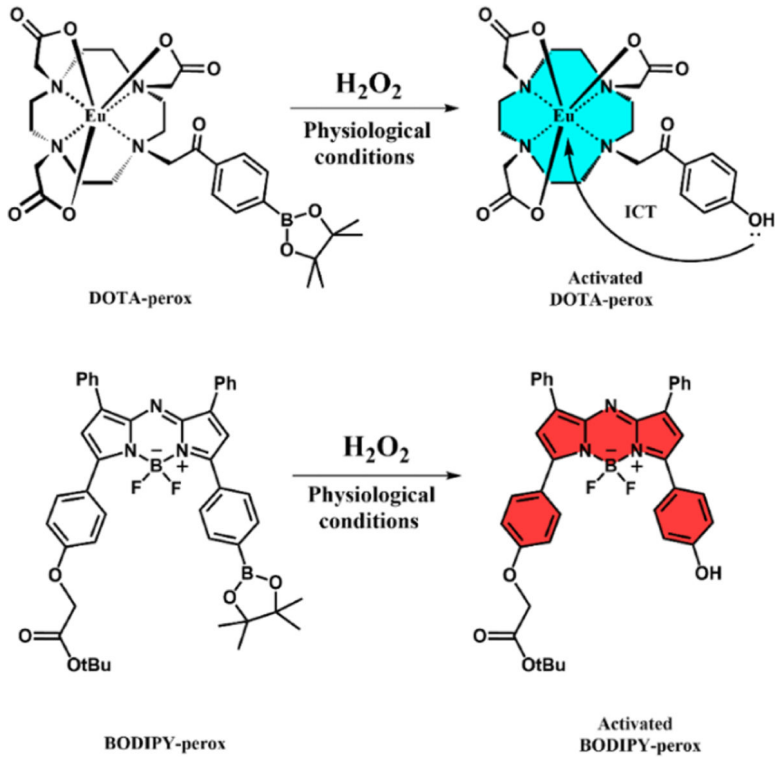

Scheme 2.

Design strategies for H_2O_2-activatable multimodal probes (**DOTA-perox** and **BODIPY-perox**). Expected reductive reaction activation of **DOTA-perox** and **BODIPY-perox** by hydrogen peroxide (H_2O_2).

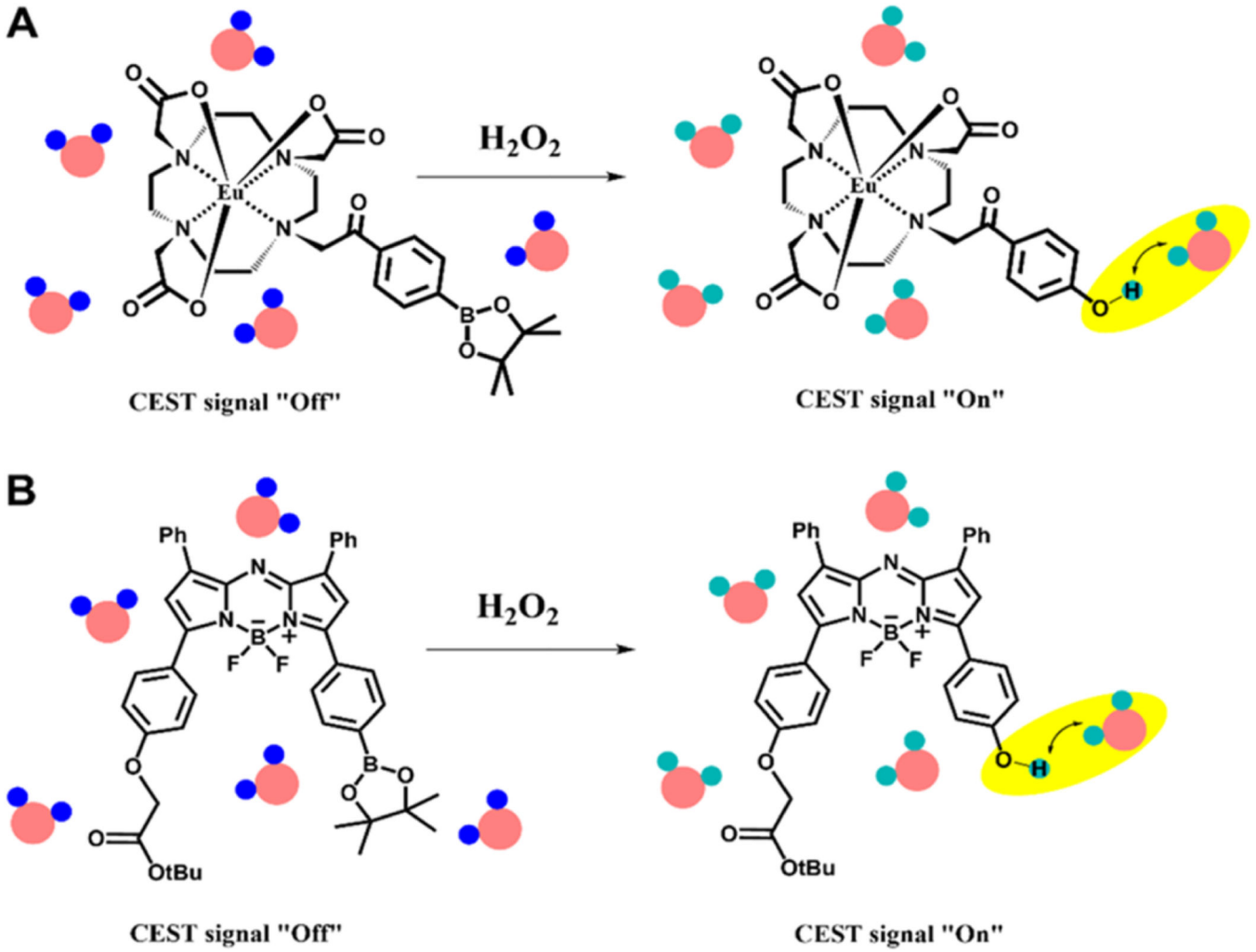

Scheme 3.

Schematic representation of the H_2O_2 activation process, CEST MRI detection of multimodal probes **DOTA-perox** (A) and **BODIPY-perox** (B). The probes are reduced by hydrogen peroxide (H_2O_2) containing exchangeable phenolic OH protons, leading to the saturation of surrounding water protons and the activation of the CEST MRI signal. See the text for further discussion.